

# A tightly coupled electromagnetic-triboelectric hybrid generator for wind energy harvesting and environmental monitoring

Hanlin Zhou<sup>a,b,c</sup>, Zhi Cao<sup>a,b,c</sup>, Zhong Lin Wang<sup>a,b,c,d</sup>,  
Zhiyi Wu<sup>a,b,c,\*</sup>

<sup>a</sup> Guangzhou Institute of Blue Energy, Knowledge City, Huangpu District, Guangzhou 510555, PR China

<sup>b</sup> Beijing Institute of Nanoenergy and Nanosystems, Chinese Academy of Sciences, Beijing 101400, PR China

<sup>c</sup> School of Nanoscience and Engineering, University of Chinese Academy of Sciences, Beijing 100049, PR China

<sup>d</sup> School of Materials Science and Engineering, Georgia Institute of Technology, Atlanta, GA 30332-0245, USA

## ARTICLE INFO

### Keywords:

Triboelectric nanogenerator  
Electromagnetic generator  
Hybrid generator  
Wind energy  
Environmental monitoring

## ABSTRACT

Small distributed wind harvesters, offering flexible deployment, lower costs, and localized power, complement large wind turbines in wind energy utilization. This paper reports a tightly coupled electromagnetic-triboelectric hybrid generator (ETHG). The electromagnetic generator (EMG) component changes the magnetic field by rotating the magnetizing material, while the magnet and coil remain stationary to facilitate close integration with the triboelectric nanogenerator (TENG) component. Furthermore, the output performance of the TENG component is optimized by studying friction materials and electrode. Finally, at a wind speed of 18.28 m/s, the TENG and EMG components can provide open-circuit voltages of 936 V and 10.35 V, and short-circuit currents of 29.6  $\mu$ A and 4.27 mA, respectively, and can charge a 3.3 mF commercial capacitor to 3.5 V in just 12.1 s. Additionally, the self-powered environmental temperature and humidity monitoring system assisted by the ETHG can continuously transmit environmental temperature and humidity information to receiver at 3-s intervals. This study provides guidance for distributed energy harvesting and has broad application prospects in environmental monitoring and self-powered sensor networks.

## Introduction

Wind energy is a non-polluting and abundant renewable resource. As global energy demand rapidly increases and energy pollution worsens, wind energy has become a key focus in the global development of green energy [1,2]. Currently, wind energy is mainly harnessed through large wind turbines that convert wind into electricity [3,4]. These turbines have a large volume and high energy output, but they require complex infrastructure and maintenance, which leads to limitations in cost and applicability. In contrast, small distributed wind energy harvesters can be more flexibly deployed in various environments such as urban buildings, rural areas, or offshore platforms. They utilize local wind resources to power small devices like distributed sensors and environmental monitoring equipment, effectively reducing power transmission losses. Therefore, with features like easy installation, strong adaptability, and high energy utilization efficiency, small distributed wind energy harvesters can serve as an important supplement in the field of wind energy utilization [5].

The triboelectric nanogenerator (TENG) is a new type of micro energy harvester that can effectively convert environmental mechanical energy into electrical energy based on the coupling of triboelectrification and electrostatic induction, especially for widely distributed, low-frequency, and irregular environmental energy [6–9]. Due to its small size, low cost, and simple structure, TENG has quickly attracted widespread attention from researchers [10–15]. In recent years, there have been numerous research results around the structural design [16–18], material optimization [19–21], and energy management of TENGs [22–25]. Meanwhile, TENG has different output characteristics from conventional electromagnetic generators (EMG). TENG has high impedance and can generate high voltage but with low current [26–30], while EMG has low impedance and can generate high current but with low voltage [30–34]. Coupling TENG with EMG can combine the advantages of both, forming a hybrid power generation system that provides both high voltage and high current. This coupling method maximizes the complementary strengths of TENG and EMG, thereby enhancing the overall energy output efficiency of the system [35–40].

\* Corresponding author at: Guangzhou Institute of Blue Energy, Knowledge City, Huangpu District, Guangzhou 510555, PR China.

E-mail addresses: [zlwang@gatech.edu](mailto:zlwang@gatech.edu) (Z.L. Wang), [wuzhiyi@binn.cas.cn](mailto:wuzhiyi@binn.cas.cn) (Z. Wu).

In this study, a high-performance triboelectric-electromagnetic hybrid generator (ETHG) is proposed for wind energy harvesting and environmental monitoring. The EMG component induces magnetic field variation by rotating a magnetically conductive material to alter the magnetic circuit path, while the magnet and coil remain fixed to enhance coupling with the TENG component. The output performance of TENG components is optimized through research on friction material types, contact conditions, and electrode design. Additionally, an energy management circuit was introduced, improving the charging performance of the TENG by 7.6 times. Finally, at a wind speed of 18.28 m/s, the TENG and EMG can provide open-circuit voltages of 936 V and 10.35 V, and short-circuit currents of 29.6  $\mu$ A and 4.27 mA, respectively, and it takes only 12.1 s to charge a 3.3 mF commercial capacitor to 3.5 V. Furthermore, a self-powered ambient temperature and humidity

monitoring system was constructed with the assistance of the ETHG, which directly captures ambient wind energy and continuously sends temperature and humidity data to the receiver at 3-s intervals. The ETHG has broad application potential in distributed energy systems, environmental monitoring, and self-powered sensor networks.

### Result and discussion

#### Structure of the ETHG

Wind energy is a renewable resource with great potential. As shown in Fig. 1a, we developed an ETHG to harvest environmental wind energy for powering various devices. Fig. 1b shows its overall appearance. The ETHG consists of two rotors at the top and bottom, and a stator in the

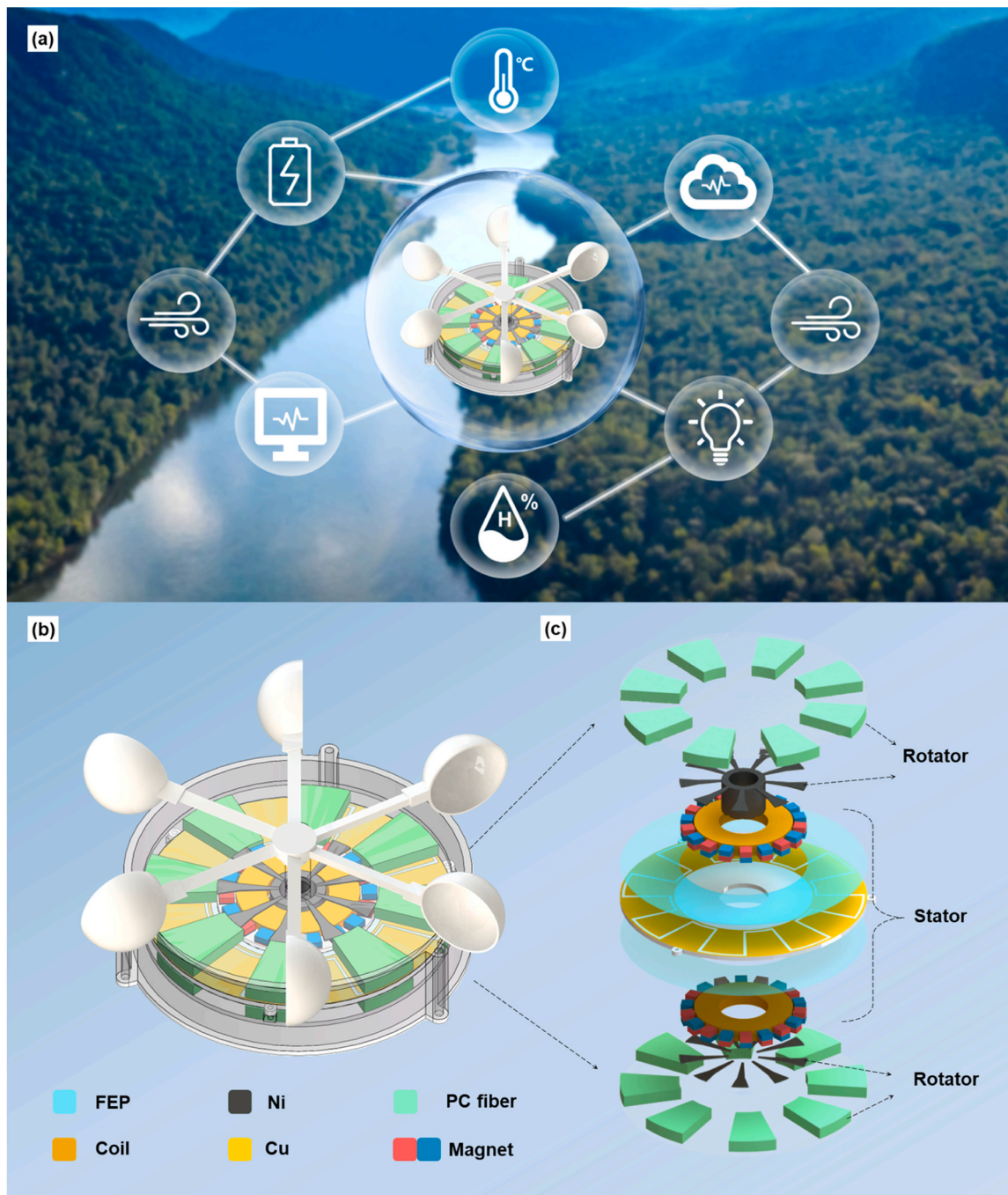


Fig. 1. a) Application outlook diagram of ETHG. b) Schematic diagram of the overall structure of ETHG. c) Schematic diagram of structural explosion of ETHG.

middle. The rotors include the TENG friction material, polycarbonate fiber (PC fiber), and the EMG magnetic conductive material, Ni. The stator includes the EMG coils and a ring of alternating magnetic poles, along with the other TENG friction material, FEP, and Cu interdigitated electrodes. Fig. 1c, S1 provides an exploded view and photo of the ETHG for a clearer visualization of the hybrid generator.

### Structure, principle and performance of the EMG component

The overall structure of the EMG component prepared in this study is shown in Fig. 2a. It consists of a ring of alternating magnetic poles, upper and lower coils, and a magnetic conductor. The magnetic conductor is composed of upper and lower magnetic conductive plates arranged in a circumferential array, along with a central magnetic conductive tube. Traditional EMG generators typically generate electricity by changing the position of the magnets to alter the magnetic field distribution, inducing an electromotive force in the coils. In this study, the EMG generates electricity by rotating the magnetic conductor to change the magnetic circuit path, thereby altering the magnetic field. Both the magnet and the coil remain fixed, allowing for more flexible arrangement, which facilitates better coupling with the TENG component. Fig. 2b(i-iii) shows the simulation results of this process using COMSOL Multiphysics software. Initially, the magnetic conductive plates made of Ni completely cover the left magnet. The magnetic circuit starts from the N pole at the top of the magnet, passes through the upper magnetic

conductive plate, converges at the central magnetic conductive tube, and then returns to the S pole at the bottom of the magnet. As the magnetic conductor rotates to the middle between the two magnets, the magnetic circuit starts from the N pole of the left magnet, passes through the upper magnetic conductive plate, and directly returns to the S pole of the right magnet, with almost no magnetic field lines passing through the central magnetic conductive tube. During this process, the downward magnetic flux at the center of the coil gradually decreases, inducing a current. Finally, as the magnetic conductor continues to rotate and completely covers the right magnet, the magnetic circuit starts from the N pole at the bottom of the magnet, pass through the lower magnetic conductive plate, converge at the central magnetic conductive tube, and then return to the S pole at the top of the magnet through the upper magnetic conductive plate. During this process, the upward magnetic flux at the center of the coil gradually increases, inducing another current. As the magnetic conductor continuously rotates, the induced current is also continuously generated, converting mechanical energy into electrical energy. The simulation results of induced voltage waveform and magnetic flux density distribution are shown in Fig. S2 and Movie S1.

Supplementary material related to this article can be found online at [doi:10.1016/j.nantod.2024.102628](https://doi.org/10.1016/j.nantod.2024.102628).

Since the output of the EMG is derived from changes in the magnetic circuit, the tighter the connection between the upper and lower magnetic conductive plates and the central magnetic conductive tube, the

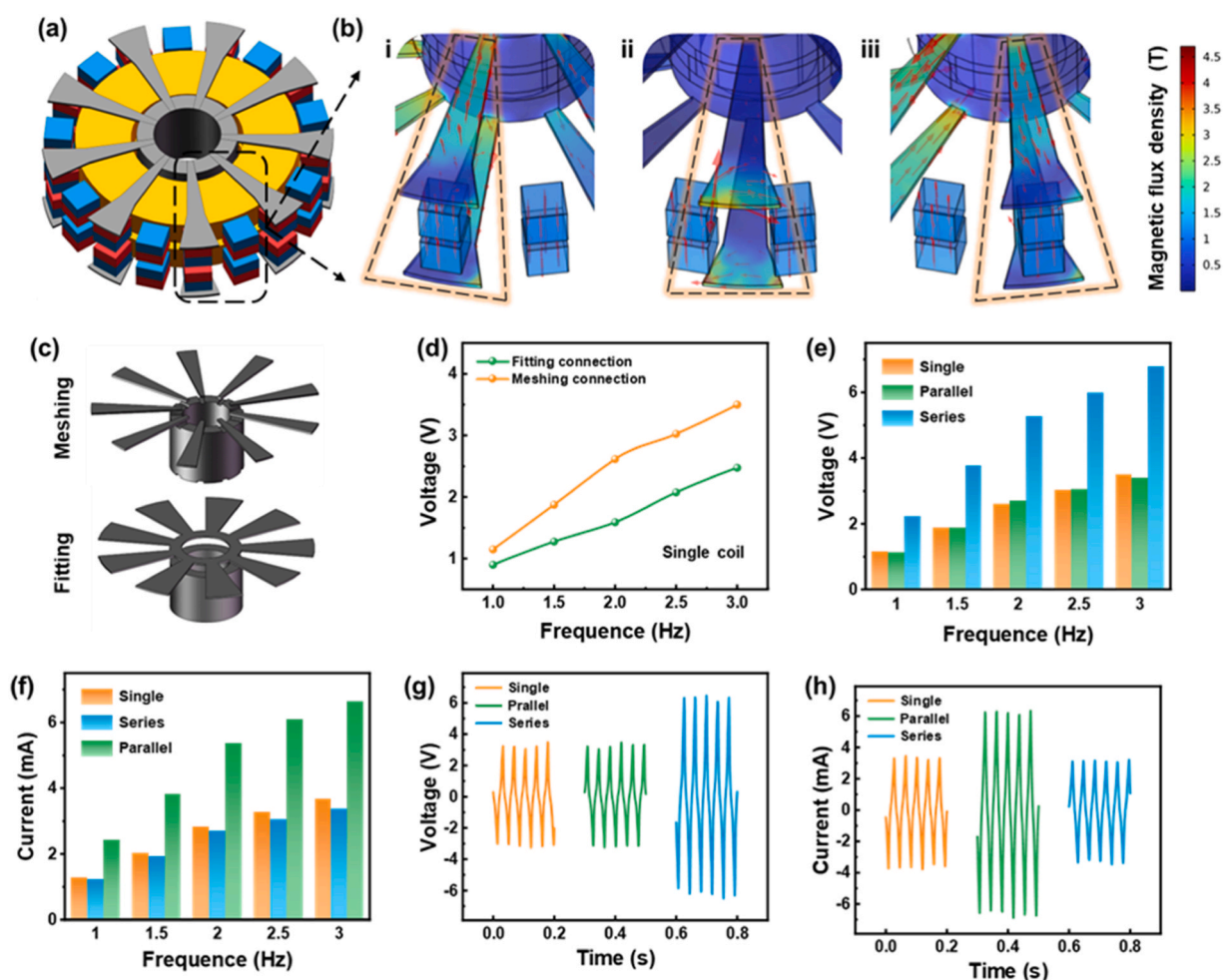


Fig. 2. a) Schematic of the overall structure of the EMG. b) Simulation of the flux density distribution of the EMG at different rotation angles. c) Schematic diagrams of the two different connection methods of the magnet-conducting material. d) Comparison of the voltage output of the EMG for the two different magnet-conducting connection methods. e, f) Comparison of the voltage, current of the EMG for the different connection methods of the coil. g, h) Waveforms of voltage and current of EMG at 3 Hz speed.

more effective the magnetic circuit will be. As shown in Fig. 2c, this study prepared magnetic conductors connected by two methods: Meshing and Fitting. The comparison of output voltage and current is shown in Fig. 2d and Fig. S3. Because the meshing method provides a tighter connection than direct fitting, its output performance is higher. Meanwhile, the device includes two coils, top and bottom, and the connection of the coils can be changed between series and parallel according to the needs to provide higher voltage or current. Fig. 2e, f shows the output effects of different coil connection methods. In parallel, the coils provide higher current, while in series, they provide higher voltage. At a rotation frequency of 3 Hz, the series connection of the coils can provide an AC voltage of +6.47 V and -6.51 V, while the parallel connection can provide an AC current of +6.34 mA and -6.49 mA, with the output waveforms shown in Fig. 2g, h. Finally, the output of the EMG under different external resistances was tested using the parallel coils at a rotation frequency of 3 Hz, and the results are shown in Fig. S4. Initially, the peak power of the coils increases with the load, reaching a maximum of 6.1 mW at around 800 $\Omega$ , and then begins to decrease as the resistance increases further, dropping to 0 at 10 k $\Omega$ .

### Structure, principle and performance of the TENG component

The overall structure of the TENG component is shown in Fig. 3a. PC fiber, which has high triboelectric performance and good durability, was selected to make the upper and lower rotors. The stator consists of Cu interdigitated electrodes arranged in a circular array and FEP film

attached to the electrodes. Due to friction with the FEP film, the PC fiber loses electrons and becomes positively charged. According to the principle of electrostatic induction, induced charges are generated on the interdigitated electrodes, creating a potential difference between the two electrodes, as shown in the simulation results in Fig. 3b. As the PC fiber rotates, the induced charges change accordingly, with the complete process shown in Movie S2. To more clearly demonstrate the charge transfer process between the two electrodes, Fig. 3c(i-iii) was drawn to explain the principle of charge transfer. Initially, when the PC fiber and FEP film come into contact, based on the contact electrification principle, the PC fiber becomes positively charged, and the FEP film becomes negatively charged. Although the total charge on both is equal, the charge density on the PC fiber is twice that of the FEP film due to its smaller contact area. According to the principle of electrostatic induction, corresponding induced charges are generated on the interdigitated electrodes, and the potential difference between the two electrodes reaches its maximum at this point. As the PC fiber gradually rotates to the middle of the two electrodes, the induced charges redistribute with the rotation, moving from the left electrode to the right electrode through the external circuit, and the potential difference between the two electrodes becomes zero. Finally, when the PC fiber rotates to the right electrode, all induced charges transfer from the left electrode to the right electrode through the external circuit, and the potential difference between the two electrodes reaches its maximum again. The simulation results of the potential difference are shown in Fig. S5.

Supplementary material related to this article can be found online at

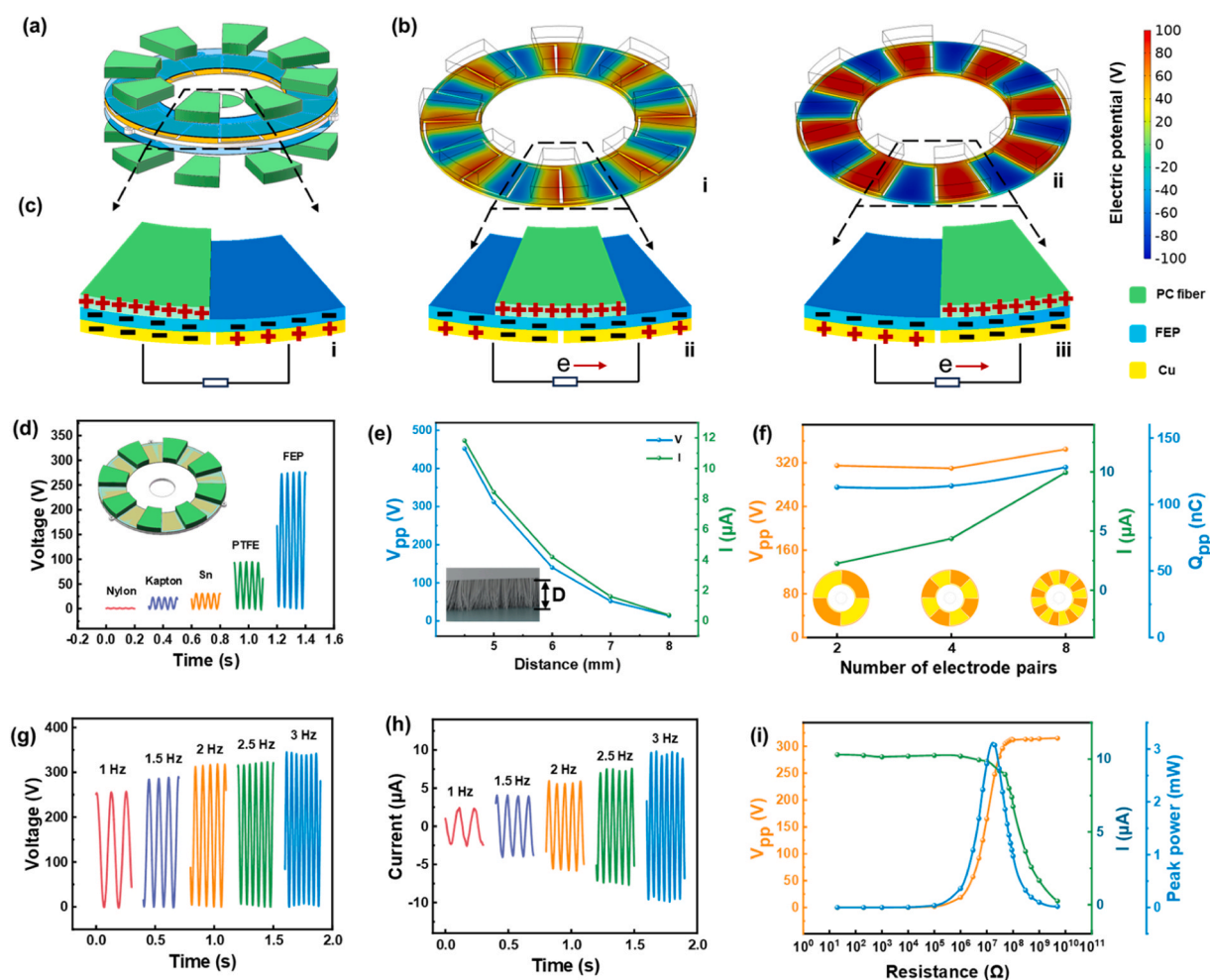


**Fig. 3.** a) Overall schematic of TENG. b) Simulated potential distribution of TENG under different rotation angles. c) Charge transfer schematic of TENG. d, e, f) Comparison of TENG output under different friction materials, distances, and electrode logarithms. g, h) Voltage and current waveforms at different frequencies. i) Peak output of TENG at different load resistances.

doi:10.1016/j.nantod.2024.102628.

There are many factors that influence the output performance of TENG. This study investigates the main factors such as the type and contact degree of friction materials, as well as the number of interdigitated electrode pairs. The potential difference in TENG comes from the charge transfer between the friction materials. The greater the difference in electronegativity between the friction materials, the better the output performance of TENG. Five common friction materials were tested in this study (Fig. 3c). Since PC fiber has lower electronegativity, the FEP with higher electronegativity produced the highest voltage. The contact degree between the friction materials is also a key factor affecting the output performance of TENG. We adjusted the distance between the rotor and stator to change the contact degree between the friction materials. Fig. 3e shows the output performance of TENG at different distances. The TENG with a rotor-stator distance of 4.5 mm achieved the highest voltage and current because the closer the distance between the rotor and stator, the more sufficient the contact between the friction materials, leading to higher output. We further tested the impact of the number of electrode pairs on performance. As shown in Fig. 3f, with an increase in the number of electrode pairs, the time to transfer the same amount of charge decreases, resulting in a continuous increase in short-circuit current. Meanwhile, since the contact area remains unchanged, the transferred charge of TENG remains almost the same, so the open-circuit voltage remains largely unchanged. Fig. 3g, h shows the waveforms of open-circuit voltage and short-circuit current of TENG at different rotational speeds. In addition, we tested the output of TENG under different loads, as shown in Fig. 3i. Initially, the peak power of the

coil increases with the load, reaching a maximum value of 3.0 mW at around 20 M $\Omega$ , after which the power begins to decrease, dropping to 0 at 5 G $\Omega$ . Finally, the TENG component was configured with PC fiber and FEP film as the friction materials, a rotor-stator distance of 4.5 mm, and 8 electrode pairs.

#### Performance and application demonstration of the ETHG

Next, the output performance of the ETHG is presented. Since the upper and lower TENGs operate synchronously, they can be directly connected in parallel for output. At a rotational speed of 3 Hz, the parallel-connected TENGs can directly provide an open-circuit voltage of 809 V, a short-circuit current of 22.8  $\mu$ A, and a transferred charge of 0.3  $\mu$ C, as shown in the waveforms in Figs. 4a, 4b, and S6. The torque required to drive the ETHG at different rotational speeds was also tested (Fig. 4c). The maximum torque required for the ETHG to operate at rotational speeds of 1, 2, and 3 Hz was 0.242, 0.303, and 0.332 N·m, respectively. In addition, we also conducted durability tests on the devices. The durability results of ETHG are shown in Fig. S7. After running continuously for approximately 10,000 cycles at 3 Hz, the TENG shows a slight degradation of about 4.46 %, which can be attributed to the use of the durable material, PC fiber. The EMG shows almost no degradation (0.3 %), which is to be expected, as numerous previous studies have demonstrated the durability of EMG. Subsequently, the charging rate of ETHG for commercial capacitors was investigated. First, charging tests were conducted on different capacitors using the EMG component with series-connected coils after full-bridge rectification, as shown in Fig. 4d.

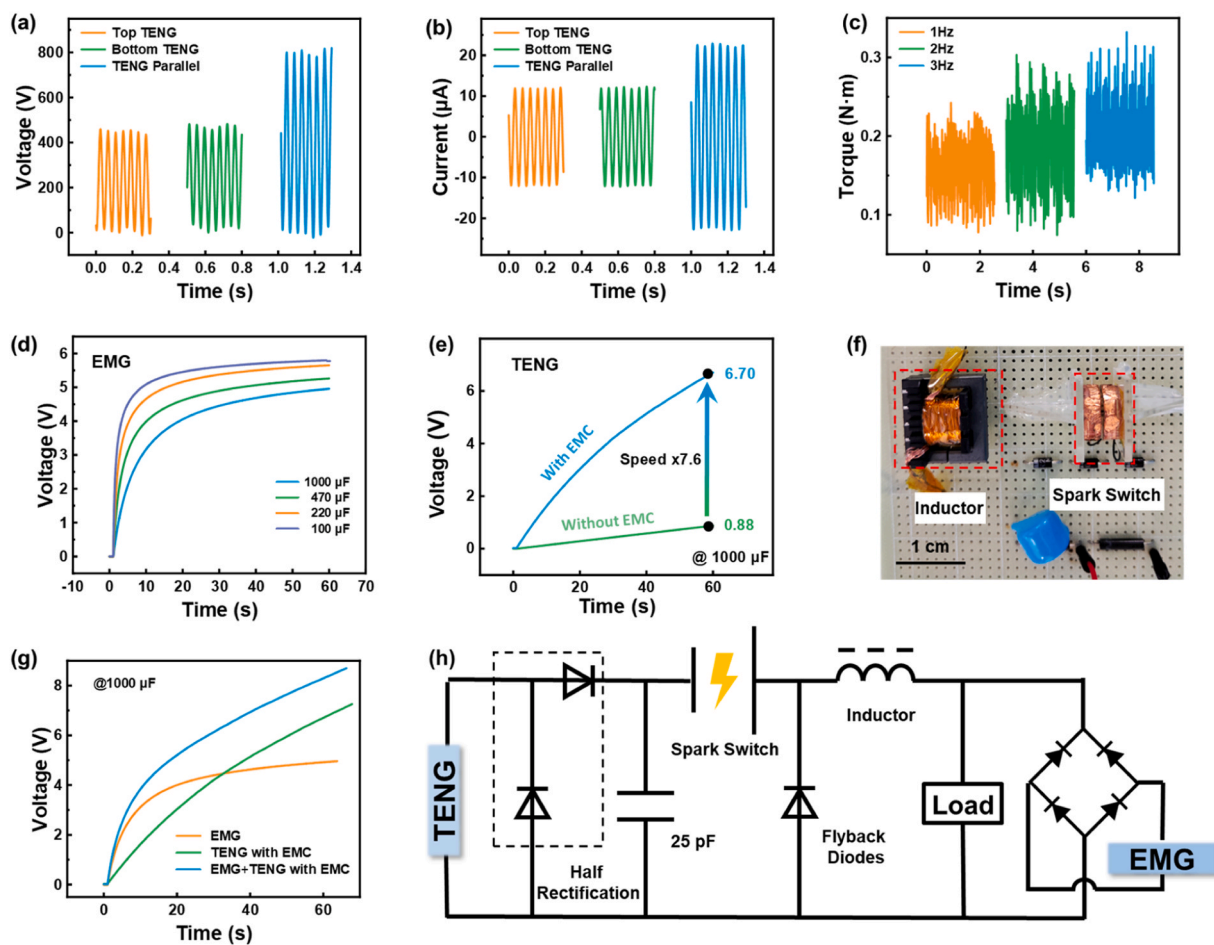


Fig. 4. a, b) Voltage, current waveforms of TENG component. c) Torque required for different rotational frequencies of ETHG. d) Charging voltage graph of EMG for different capacitors e) Comparison of the charging speed of capacitors by TENG with and without energy management circuit (EMC) connected. f) Photographs of EMC. g) Comparison of the charging speed of the capacitors by EMG component, TENG component, and both together. h) Circuit diagram of EMC.

Initially, the capacitor voltage rises rapidly, and as the capacitor voltage approaches the rectified voltage of the EMG, the charging rate gradually decreases until the capacitor voltage stabilizes. Then, the charging efficiency of the TENG component was explored (Fig. 4e). Due to the significant difference in matching impedance between the TENG and commercial capacitors, we referred to related literature and introduced the power management circuit shown in Fig. 4f, 4h, which increased the charging rate of TENG by 7.6 times. Finally, as shown in Fig. 4g, the ETHG combines the complementary advantages of EMG and TENG. The EMG improves the charging rate of the TENG when the capacitor voltage is low, while the TENG overcomes the maximum charging voltage limitation of the EMG, allowing a 1 mF capacitor to be charged to 8 V within 60 s.

Global warming is becoming increasingly severe, making it essential to monitor environmental temperature and humidity. This study developed a self-powered environmental temperature and humidity monitoring system based on ETHG. The system harnesses wind energy through ETHG to power a capacitor, which then drives a wireless temperature and humidity sensor to transmit environmental data to a receiver. Fig. 5a, b shows the workflow diagram and the physical photo of the monitoring system. First, we tested the wind energy harvesting capability of the ETHG. As shown in Fig. 5c, d, at a wind speed of 18.28 m/s, the TENG component can directly provide an open-circuit voltage of 936 V and a short-circuit current of 29.6  $\mu$ A, while the EMG component can directly provide an open-circuit voltage of 10.35 V and a short-circuit current of 4.27 mA. Then, the ETHG connected a 3.3 mF capacitor and a wireless temperature and humidity sensor through a power management circuit. When the ETHG started operating, the

capacitor was charged to the working voltage of 3.5 V in just 12.1 s, and the sensor began collecting environmental temperature and humidity data. The Bluetooth module then activated and connected to a smartphone, successfully transmitting the data containing the environmental information. Finally, the monitoring system continued to operate, sending data to the smartphone at 3-s intervals. The entire process is recorded in Movie S3 in the supporting information, and the voltage waveform of the system is shown in Fig. 5e.

Supplementary material related to this article can be found online at [doi:10.1016/j.nantod.2024.102628](https://doi.org/10.1016/j.nantod.2024.102628).

## Conclusion

In conclusion, this study designed a small-sized, high-performance ETHG. The EMG component changes the direction of the magnetic circuit by rotating the magnetic conductive material, thereby causing variations in the magnetic field, while the magnet and coil remain fixed, allowing better coupling with the TENG component. Additionally, by studying the types of friction materials, the degree of contact, and the electrode design, the output performance of the TENG component was optimized. A power management circuit was also introduced, improving the charging performance of the TENG by 7.6 times. The ETHG combines the complementary advantages of EMG and TENG, with EMG improving the charging rate of TENG at low capacitor voltages and TENG overcoming the maximum charging voltage limitation of EMG, enabling a 1 mF capacitor to be charged to 8 V within 60 s at a frequency of 3 Hz. Finally, with the help of ETHG, a self-powered environmental temperature and humidity monitoring system was developed. At a wind

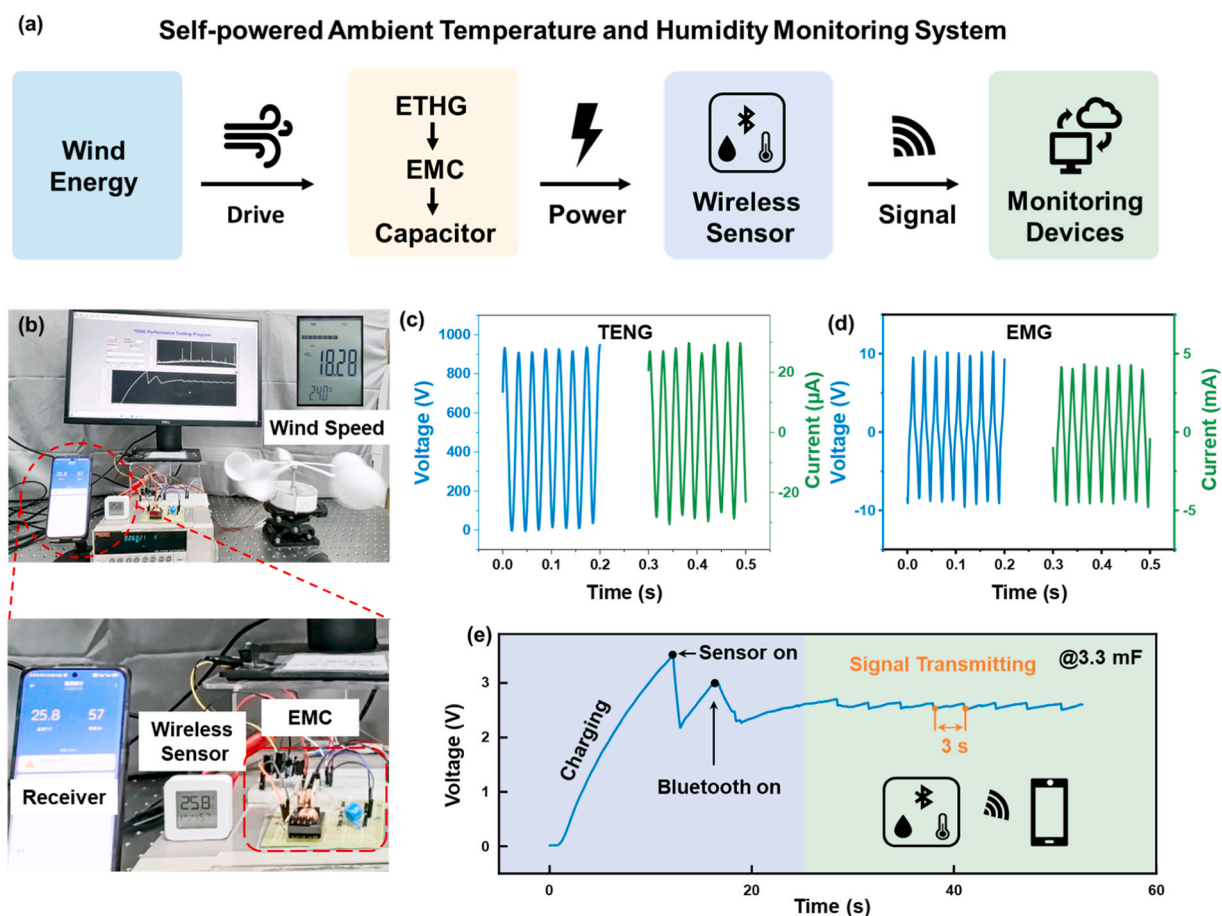


Fig. 5. a) Schematic illustration of the self-powered wireless environment monitoring system. b) A photo of the wind-powered wireless temperature and humidity sensing system. c, d) Open circuit voltage and short circuit current of TENG and EMG. e) Voltage curve of a 3.3 mF commercial capacitor when powering the temperature and humidity monitor system.

speed of 18.28 m/s, the system can continuously transmit environmental temperature and humidity information to the receiver at 3-s intervals. This hybrid generator, combining TENG and EMG, shows significant potential for development in areas such as distributed energy systems, environmental monitoring, and self-powered sensor networks.

## Experimental section

**Fabrication of the ETHG:** The upper rotor consists of the base, PC fibers, magnetic conductive plates, and magnetic conductive tube. The base is an acrylic disk with a diameter of 100 mm and a thickness of 2 mm. The PC fibers, each with a length of 8 mm, are cut into 8 fan-shaped segments (with a central angle of  $22.5^\circ$ , an inner diameter of 56 mm, and an outer diameter of 100 mm), arranged in a circumferential array. The dimensions of the upper magnetic conductive plates are shown in Fig. S1d; these plates have a thickness of 0.5 mm, are made of Ni, and are arranged in a circumferential array with a total of 9 plates. The magnetic conductive tube has an inner diameter of 12 mm, an outer diameter of 18 mm, and a length of 14 mm, with grooves on the upper and lower end surfaces designed to engage with the tips of the magnetic conductive plates. The lower rotor is identical to the upper rotor except that it does not include the magnetic conductive tube.

The stator comprises the support, electrodes of TENG, FEP films, magnetic rings, and coil. The support is an acrylic disk with an inner diameter of 20 mm, an outer diameter of 100 mm, and a thickness of 2.5 mm. The electrodes are 1 mm thick copper-clad Printed Circuit Board (PCB) with an inner diameter of 56 mm, an outer diameter of 100 mm, copper thickness is  $35\ \mu\text{m}$ , and a surface coating of  $10\ \mu\text{m}$  of tin to prevent oxidation. The FEP film is adhered to the surface of the electrodes (inner diameter of 56 mm, outer diameter of 100 mm, thickness of  $50\ \mu\text{m}$ ). The magnetic rings consist of NdFeB magnets arranged in an alternating circumferential array with 18 magnetic poles, each with dimensions of  $5 \times 5 \times 5\ \text{mm}$  and a surface magnetic field strength of 387 GS. The coil has an inner diameter of 20 mm, an outer diameter of 40 mm, a height of 5 mm, a turn of 3600, and a wire gauge of 0.1 mm.

**Power management circuit:** The power management circuit consisted of a half rectifier bridge, a 25 pF capacitor for storing charge, a spark switch, an inductor, and flyback diodes. The high voltage diode (2CL77) is used for half rectification and the flyback diode is made by connecting three R2000 in series. The spark switch is made up of two copper pieces of 10 mm and 12 mm diameter with a gap of 1.5 mm, the inductor is made of an EE22 type magnetic core and  $0.1 \times 20\ \text{mm}$  copper wire with a coil number of 72.

**Electric Measurements of the ETHG:** The output performance of the ETHG, including voltage, current, and transferred charge, was measured using a static electrometer (Keithley 6514), a data acquisition card (NI PCI-6255), and the LabVIEW software platform. The constant-frequency rotation and torque measurements were provided by a rotary linear motor (LinMot-E1200). Wind generation was achieved with a commercial blower, and wind speed was measured using an anemometer (San-Liang RA620). The wireless sensor employed was the Xiaomi Bluetooth Thermo-Hygrometer (LYWSD03MMC).

## CRedit authorship contribution statement

**Hanlin Zhou:** Writing – review & editing, Writing – original draft, Visualization, Software, Methodology, Formal analysis, Data curation, Conceptualization. **Zhi Cao:** Visualization, Software, Methodology, Formal analysis, Data curation. **Zhong Lin Wang:** Writing – review & editing, Supervision, Project administration, Funding acquisition. **Zhiyi Wu:** Writing – review & editing, Supervision, Resources, Project administration, Investigation, Funding acquisition, Formal analysis, Conceptualization.

## Declaration of Competing Interest

The authors declare that they have no known competing financial interests or personal relationships that could have appeared to influence the work reported in this paper

## Acknowledgments

H.Z. and C.Z. contributed equally to this work. The research was supported by the National Key R and D Project from Minister of Science and Technology (2021YFA1201604).

## Appendix A. Supporting information

Supplementary data associated with this article can be found in the online version at doi:10.1016/j.nantod.2024.102628.

## Data availability

Data will be made available on request.

## References

- [1] J. Eom, M. Hyun, J. Lee, H. Lee, *Nat. Energy* 5 (2020) 976–984.
- [2] S. Chu, A. Majumdar, *Nature* 488 (2012) 294–303.
- [3] T. Macquart, A. Maheri, *Renew. Energy* 133 (2019) 964–970.
- [4] Z. Jiang, *Renew. Sustain. Energy Rev.* 139 (2021) 110576.
- [5] A. Tummala, R.K. Velamati, D.K. Sinha, V. Indrajha, V.H. Krishna, *Renew. Sustain. Energy Rev.* 56 (2016) 1351–1371.
- [6] F.-R. Fan, Z.-Q. Tian, Z. Lin Wang, *Nano Energy* 1 (2012) 328–334.
- [7] Z.L. Wang, A.C. Wang, *Mater. Today* 30 (2019) 34–51.
- [8] S. Niu, Y. Liu, S. Wang, L. Lin, Y.S. Zhou, Y. Hu, Z.L. Wang, *Adv. Mater.* 25 (2013) 6184–6193.
- [9] S. Niu, Y. Liu, X. Chen, S. Wang, Y.S. Zhou, L. Lin, Y. Xie, Z.L. Wang, *Nano Energy* 12 (2015) 760–774.
- [10] W. Xu, H. Zheng, Y. Liu, X. Zhou, C. Zhang, Y. Song, X. Deng, M. Leung, Z. Yang, R. X. Xu, Z.L. Wang, X.C. Zeng, Z. Wang, *Nature* 578 (2020) 392–396.
- [11] Y. Su, G. Chen, C. Chen, Q. Gong, G. Xie, M. Yao, H. Tai, Y. Jiang, J. Chen, *Adv. Mater.* 33 (2021) 2101262.
- [12] H. Li, J. Wen, Z. Ou, E. Su, F. Xing, Y. Yang, Y. Sun, Z.L. Wang, B. Chen, *Adv. Funct. Mater.* 33 (2023) 2212207.
- [13] Z. Zhou, X. Li, Y. Wu, H. Zhang, Z. Lin, K. Meng, Z. Lin, Q. He, C. Sun, J. Yang, Z. L. Wang, *Nano Energy* 53 (2018) 501–507.
- [14] S. Liu, Y. Liu, Y. Chen, S. Wang, C. Men, S. Gao, *ACS Appl. Mater. Interfaces* 14 (2022) 17426–17433.
- [15] Y. Wang, Z. Qian, C. Zhao, Y. Wang, K. Jiang, J. Wang, Z. Meng, F. Li, C. Zhu, P. Chen, H. Wang, M. Xu, *Adv. Mater. Technol.* 8 (2022) 2201245.
- [16] P. Chen, J. An, S. Shu, R. Cheng, J. Nie, T. Jiang, Z.L. Wang, *Adv. Energy Mater.* 11 (2021) 2003066.
- [17] J. Han, Y. Feng, P. Chen, X. Liang, H. Pang, T. Jiang, Z.L. Wang, *Adv. Funct. Mater.* 32 (2021) 2108580.
- [18] C. Zhang, Y. Liu, B. Zhang, O. Yang, W. Yuan, L. He, X. Wei, J. Wang, Z.L. Wang, *ACS Energy Lett.* (2021) 1490–1499.
- [19] B. Wang, X. Zhai, X. Wei, Y. Shi, X. Huo, R. Li, Z. Wu, Z.L. Wang, *Nano Res.* 15 (2022) 8435–8441.
- [20] X. Wei, B. Wang, Z. Wu, Z.L. Wang, *Adv. Mater.* 34 (2022) 2203073.
- [21] H. Xu, X. Wang, J. Niu, Y. Nan, J. Pu, H. Zhou, J. Duan, Y. Huang, B. Hou, *Adv. Mater. Interfaces* 9 (2022) 2102085.
- [22] L. Xu, H. Wu, G. Yao, L. Chen, X. Yang, B. Chen, X. Huang, W. Zhong, X. Chen, Z. Yin, Z.L. Wang, *ACS Nano* 12 (2018) 10262–10271.
- [23] Y. Dai, G. Liu, J. Cao, B. Fan, W. Zhou, Y. Li, J. Yang, M. Li, J. Zeng, Y. Chen, Z. L. Wang, C. Zhang, *Adv. Sci.* 11 (2024) 2404253.
- [24] Z. Wang, W. Liu, J. Hu, W. He, H. Yang, C. Ling, Y. Xi, X. Wang, A. Liu, C. Hu, *Nano Energy* 69 (2020) 104452.
- [25] Z. Wang, Q. Tang, C. Shan, Y. Du, W. He, S. Fu, G. Li, A. Liu, W. Liu, C. Hu, *Energy Environ. Sci.* 14 (2021) 6627–6637.
- [26] H. Zhou, X. Wei, B. Wang, E. Zhang, Z. Wu, Z.L. Wang, *Adv. Funct. Mater.* 33 (2022) 2210920.
- [27] F. Liu, Y. Liu, Y. Lu, Z. Wang, Y. Shi, L. Ji, J. Cheng, *Nano Energy* 56 (2019) 482–493.
- [28] C. Hao, Z. Wang, M. Cai, T. Liu, C. Zhai, J. Cui, Y. Zheng, C. Xue, *Nano Energy* 128 (2024) 109857.
- [29] J. Nie, X. Chen, Z.L. Wang, *Adv. Funct. Mater.* 29 (2018) 1806351.
- [30] J. Liu, L. Zhou, Y. Gao, P. Yang, D. Liu, W. Qiao, B. Zhang, Z. Zhao, Z.L. Wang, J. Wang, *Adv. Energy Mater.* 13 (2023) 2300410.
- [31] Z. Li, X. Jiang, W. Xu, Y. Gong, Y. Peng, S. Zhong, S. Xie, *Energy* 258 (2022) 124759.
- [32] X. Zhou, K. Wang, S. Li, Y. Wang, D. Sun, L. Wang, Z. He, W. Tang, H. Liu, X. Jin, Z. Li, *Appl. Energy* 353 (2024) 122075.

- [33] J.V. Vidal, P. Rolo, P.M.R. Carneiro, I. Peres, A.L. Kholkin, M.P. Soares dos Santos, *Appl. Energy* 325 (2022) 119802.
- [34] X. Pan, P. Ling, H. Bao, W. He, Q. Li, B. Yan, *Energy Convers. Manag.* 294 (2023) 117569.
- [35] F. Zheng, Y. Zhou, S. Hu, R. Li, Z.L. Wang, Z. Wu, *Adv. Energy Mater.* 12 (2022) 2201966.
- [36] Z. Cao, Z. Yuan, C. Han, J. Feng, B. Wang, Z.L. Wang, Z. Wu, *ACS Appl. Nano Mater.* 5 (2022) 11577–11585.
- [37] C. Han, Z. Cao, Z. Yuan, Z. Zhang, X. Huo, La Zhang, Z. Wu, Z.L. Wang, *Adv. Funct. Mater.* 32 (2022) 2205011.
- [38] X. Cao, H. Zhou, Y. Zhou, Y. Hu, Y. Wang, Z.L. Wang, Q. Sun, *Adv. Mater. Technol.* 8 (2023) 2300327.
- [39] M. Ding, J. Wang, D. Zhao, H. Li, X. Cheng, J. Wen, Z.L. Wang, T. Cheng, *Nano Res.* 17 (2024) 7144–7152.
- [40] C. Zhang, S. Yang, X. Dai, Y. Tu, Z. Du, X. Wu, Y. Huang, J. Fan, Z. Hong, T. Jiang, Z.L. Wang, *Nano Energy* 128 (2024) 109929.